

Strong Eddy Kinetic Energy Anomalies Induced by Baroclinic Instability in the Southwest Region of the Kerguelen Plateau, East Antarctic

Yunzhu He¹, Meng Zhou^{1,2*}, and Dujuan Kang¹

¹ School of Oceanography, Shanghai Jiao Tong University, Shanghai, China

² Key Laboratory of Polar Science, Polar Research Institute of China, Ministry of Nature Resources, China

*Correspondence to: Meng Zhou, meng.zhou@sjtu.edu.cn

Key Points

- The subpolar region to the southwest of the Kerguelen Plateau is characterized by anomalous strong Eddy Kinetic Energy (EKE) in 2017.
- The strong regional anomalies in EKE can be primarily attributed to baroclinic instability, with inverse barotropic energy conversion.
- Baroclinic instability is mainly caused by anomalous intrusion of Circumpolar Deep Water, particularly at depths between 500-2000 meters.

18 **Abstract**

19 Eddy activities are particularly prominent in the Southern Ocean due to the instabilities of
20 the Antarctic Circumpolar Current (ACC), which plays a critical role in energy transport of
21 the global ocean. The Indian sector of the Southern Ocean is not only a typical eddy-rich
22 region with strong Eddy Kinetic Energy (EKE) and associated energy conversions among
23 different energy reservoirs (kinetic energy and potential energy of the eddy and mean flow),
24 but also events of extreme EKE. In this study, a systematic energetics analysis framework is
25 employed to examine the notable anomalies of an intensified EKE event observed in the
26 southwest region of the Kerguelen Plateau in 2017 based on a reanalysis product. The EKE
27 anomaly existing at all depths emerges in April, reaches its peak during the austral winter,
28 and persists into the following summer. Energetics analysis indicates that the strong
29 anomalous EKE is primarily determined by baroclinic instability, with distinct governing
30 mechanisms at the surface and in the internal ocean. The anomalous intrusion of warm
31 Circumpolar Deep Water intensifies the baroclinic energy conversion in the subsurface,
32 which contributes to the observed EKE anomalies. Moreover, the anomalous strong wind-
33 induced Ekman pumping serves to amplify the lifting of isopycnals, which enhances the
34 baroclinic instability and subsequently intensifies the EKE anomalies. This study sheds new
35 light on underlying mechanisms governing local polar dynamics and provides insights into
36 the intricate interaction between ocean dynamics and energy distribution in the Antarctic.

37

38 **Plain Language Summary**

39 The Indian sector of the Southern Ocean is a region known for its spatiotemporal
40 variability often referred to as jets and eddies. Eddy Kinetic Energy (EKE) is widely used to
41 measure the kinetic energy as the difference between the total kinetic energy and the kinetic
42 energy of mean currents. This study finds an anomalous event of significant increases in EKE
43 in the southwest region of the Kerguelen Plateau in the Southern Ocean in 2017. We apply a
44 systematic energetics analysis framework to a reanalysis product to investigate the processes
45 responsible for the observed anomalous event. The results suggest that the main cause for the
46 event was the anomalous intrusion of warm water masses in the upper and deeper ocean
47 layers, which led to the increases in density gradients and then intensified the energy
48 conversion from available potential energy to EKE. Moreover, the change in wind pattern has
49 an impact on the variations of EKE in the upper ocean. This study provides a better
50 understanding of energy conversions and underlying mechanisms for EKE in polar regimes.

51 **Keywords**

52 Eddy Kinetic Energy; Baroclinic Instability; Circumpolar Deep Water; Antarctic
53 Circumpolar Current; Polar Dynamics

54

55 1. Introduction

56 The Southern Ocean is a critical region for the oceanic uptake of carbon and heat. It
57 exhibits substantial ocean-atmosphere momentum exchanges and is a typical region with
58 eddy-mean flow interaction [Morrow et al., 1994; Orsi et al., 1995; Chen et al., 2014;
59 Rintoul, 2018]. In the Southern Ocean, high levels of eddy activities are associated with the
60 jets and fronts of the Antarctic Circumpolar Current (ACC) [Thompson, 2008; Frenger et al.,
61 2015], which is a dominant eastward-flowing large-scale circumpolar current [Sokolov and
62 Rintoul, 2009]. Several significant ocean fronts that align with the axes of ACC jets actively
63 interact with topographic features and mesoscale eddies. The circumpolar eddy dynamics and
64 variability have a profound impact on global air-sea interactions and thermohaline circulation
65 [Gille, 1994; Hughes and Ash, 2001; Thompson, 2008; Fu et al., 2010; Hogg et al., 2015;
66 Rintoul, 2018; Hogg et al., 2022].

67 The Indian sector of the Southern Ocean is a typical eddy-rich region with various
68 energy and mass transport [Sparrow et al., 1996; Shi et al., 2002]. The Kerguelen Plateau
69 (KP), located in the middle of the Indian sector, is one of the most prominent topographic
70 features around the polar current region, exerting a substantial influence on the ACC [Webb,
71 1993; Morrow et al., 1994; Bestley et al., 2020]. In the southwest of the KP, the ACC extends
72 meridionally from the northwest, reaching its southernmost point of 65°S (Figure 1). A
73 cyclonic sub-polar gyre, the Prydz Bay Gyre (PBG), was detected near the Southern
74 Boundary (SB) of the ACC between 60° and 80°E [Smith et al., 1984; Nunes Vaz and
75 Lennon, 1996; Heywood et al., 1999]. It is located to the west of the Princess Elizabeth
76 Trough (PET), a topographic gap between the KP and the Antarctic continent [Orsi et al.,
77 1995; Heywood et al., 1999]. The interaction of currents and gyres in this region gives rise to
78 multiscale eddies, which play a crucial role in energy and momentum transport in the
79 circumpolar region. These multiscale disturbances have significant impacts on the local

ecosystem, highlighting the importance of understanding their dynamics and interactions with surrounding flows [Swadling et al., 2010; Williams et al., 2010; Mou et al., 2021].

The Southern Antarctic Circumpolar Current Front (SACCF) and the SB pass through the southern KP. It was suggested that the SACCF is steered by the topography of the KP, causing a horizontal shear between the eastward ACC and westward-flowing Antarctic Slope Current (ASC) [Meijers et al., 2010]. Additionally, it is an important upwelling region associated with the atmospheric Antarctic Divergence (AD) in the south of the ACC, which is a meteorological zone mirrored in the ocean properties between the northward and southward Ekman transports due to the westerlies and easterlies [e.g., Foldvik and Gammelsrod, 1988]. The upwelling induced by Ekman transports draws warm Circumpolar Deep Water (CDW) into the surface waters. Characterized as a salty, warm water mass in the Southern Ocean, CDW is forced across the shelf break into Prydz Bay, where it plays a crucial role in mixing processes at the continental margin [Whitworth III et al., 1985; Williams et al., 2016; Liu et al., 2017; Thompson et al., 2018]. Eddies and turbulence actively facilitate mixing along and across isopycnals in this region [Wakatsuchi et al., 1994; Rintoul, 2018].

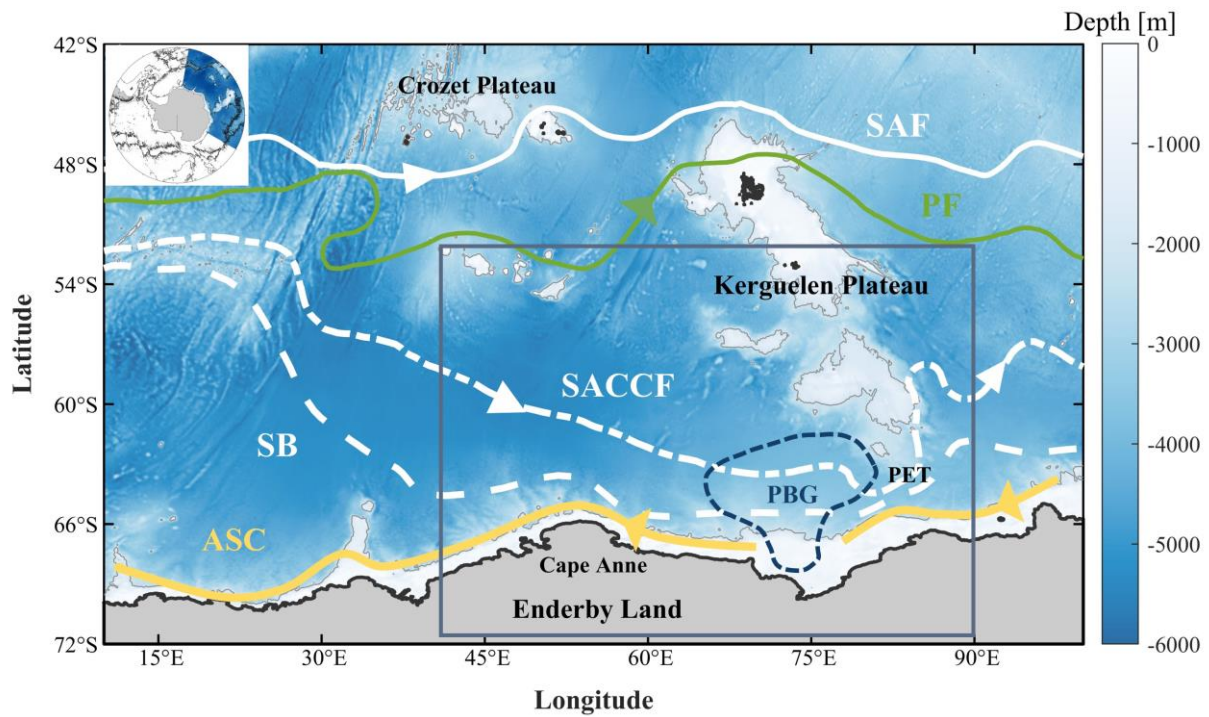


Figure 1. Schematic of bathymetry with major topography features and main currents in the Indian sector of the Southern Ocean (colored part in the inset), East Antarctica. The light grey lines indicate the isobath of 2000 m from the ETOPO1 bathymetry dataset. The historical position of the Southern Boundary (SB, white dashed line) of the ACC, Southern Antarctic Circumpolar Current Front (SACCf, white dot-dashed line), Polar Front (PF, green solid line), and Subantarctic Front (SAF, white solid line) from Orsi et al. [1995] is as shown. The schematic of the Antarctic Slope Current (ASC, yellow solid line) from Orsi et al. [1995] and the Prydz Bay Gyre (PBG) region (dark blue dashed line) from Heywood et al. [1999] are shown. The gap in the topography between the Kerguelen Plateau and the Antarctic continent (85°E, 63°-66°S) is the Princess Elizabeth Trough [Heywood et al., 1999]. The study region is indicated by the light green box in the figure.

Eddy Kinetic Energy (EKE) is widely utilized as a crucial component of the kinetic energy associated with eddies, encompassing all transient motions [Martinez-Moreno et al., 2019]. In the Southern Ocean, EKE produces a strongly heterogeneous distribution influenced by the interplay between wind forcing, topography, and mean flow [Morrow et al., 2010]. Previous studies have proposed a substantial increase in EKE within the Southern Ocean in recent decades [Hogg et al., 2015; Martinez-Moreno et al., 2019; Martinez-Moreno et al., 2022], while a recent analysis of EKE trends in smaller regions in the Southern Ocean

suggested that the changes in EKE are not uniformly distributed as previously implied, and significant EKE increase only downstream of the Campbell Plateau [Hogg et al., 2015; Zhang et al., 2021]. Numerous studies have focused on analyzing EKE to comprehend large-scale physical processes in the ACC region [Hughes and Ash, 2001; Meredith and Hogg, 2006; Trani et al., 2014; Hogg et al., 2022]. Most of these investigations have concentrated on downstream of large topographic barriers characterized by significant EKE, particularly in the KP area, based on satellite observations or numerical modeling [Morrow et al., 1994; Morrow et al., 2010; Trani et al., 2014; Rosso et al., 2015; Zhang et al., 2021; Cai et al., 2022; Shi et al., 2023]. The interactions between the ACC and subpolar gyres under the wind impact in different high-latitude regions have received significant attention due to their impacts on biological diversity and productivity in recent years. A quantitative assessment of the energy budget focused on the lee of significant topographic features in a realistic model was performed and the relative importance of localized energy conversion compared to the energy conversion across the entire ACC region was estimated [Matsuta and Masumoto, 2023]. The results demonstrated that the westerlies can locally supply sufficient energy to initiate baroclinic instability in the Indian and Pacific sectors of the ACC. In the central Pacific sector, the interannual variation of EKE in the upper ocean layer has revealed that wind stress impacts the variation through both baroclinic and barotropic pathways [Fu et al., 2023]. However, the Indian sector remains poorly explored.

A significant event of strong EKE that occurred in 2017 was observed in the confluence of SACCF and PBG region during the austral winter in the present study. Previous studies have concentrated on the anomalies in 2016-2017 in the Antarctic. Antarctic sea ice extent has been suggested to decline dramatically from September 2016, culminating in a record low by December in the austral summer, and coincided with anomalously warm surface waters surrounding most of Antarctica [Stuecker et al., 2017; Turner et al., 2017; Meehl et al., 2019;

Wang et al., 2019]. The rapid decrease of sea ice extent was attributed to sustained ocean hydrographic changes and easterly wind anomalies. The anomalous warming in the southern Indian Ocean was observed accompanied by pronounced low chlorophyll levels in Prydz Bay [Meehl et al., 2019; Sabu et al., 2021]. Notably, the EKE anomaly occurred following this regional warming. Analyzing the hydrography and dynamical processes during this specific period could provide insights into underlying mechanisms and potential connections with climate variability and oceanic changes. The reanalysis products of GLORYS12V1 data and ERA5 data were employed to examine the regional patterns of EKE in all ocean layers from the perspective of energetics analysis and to explore the causes of the anomalous event.

2. Data and Methods

The reanalysis data acquired from the Global Ocean Reanalysis and Simulation (GLORYS12V1) product were used to investigate the time-varying energetics in this study, limited by the scarcity of *in-situ* observation. This product is the Copernicus Marine Environment Monitoring Service (CMEMS) global ocean eddy-resolving ($1/12^\circ$ horizontal resolution, 50 vertical levels) reanalysis covering the altimetry (1993 onward), which has been used to analyze energetics in the Southern Ocean [Fu et al., 2023]. Utilized monthly and daily variables include sea surface height, current velocity, potential temperature, and practical salinity in all vertical levels, from 1993 to 2020.

To evaluate the performance of the reanalysis data in the study region, we compared the climatology and yearly averaged geostrophic Eddy Kinetic Energy (EKE_g) from satellite altimetry observations with the reanalysis result. The daily sea surface height (SSH) product with $0.25^\circ \times 0.25^\circ$ spatial resolution during 1993-2020 was utilized to investigate EKE_g . The

gridded Level-4 product from CMEMS were constructed by merging TOPEX/Poseidon, Jason-1/2, ERS-1/2, GFO, CryoSat-2, HY-2A, Altika, and ENVISAT mission data.

Monthly mean wind data were obtained from the European Centre for Medium-Range Weather Forecasts (ECMWF) ERA5 reanalysis fields for the period 1993-2020. They were used to understand the possible mechanisms influencing circulation patterns and eddy activities. The spatial resolution is $0.25^\circ \times 0.25^\circ$.

The wind stress is derived from

$$\boldsymbol{\tau} = \rho_a C_D |\mathbf{V}_w| \mathbf{V}_w, \quad (1)$$

where $\boldsymbol{\tau}$ is the vector wind stress, ρ_a is the density of air approximately equal to 1.22 kg m^{-3} , C_D is the drag coefficient of wind on seawater approximately equal to 1.5×10^{-3} , and \mathbf{V}_w is vector wind velocity in m s^{-1} .

The Ekman transport divergence is given by

$$\nabla \cdot U_E = \partial / \partial x (\boldsymbol{\tau}^{(y)} / (\rho f)) - \partial / \partial y (\boldsymbol{\tau}^{(x)} / (\rho f)) = \mathbf{k} \cdot \nabla \times (\boldsymbol{\tau} / \rho f), \quad (2)$$

where U_E is the vector Ekman transport, f is the Coriolis constant, $\boldsymbol{\tau}^{(x)}$ and $\boldsymbol{\tau}^{(y)}$ are x- and y-components of wind stress, respectively, \mathbf{k} is the unit vector in the vertical direction, and ∇ is the gradient operator. Therefore, in the Southern Hemisphere ($f < 0$), upwelling into the Ekman layer results from negative wind stress curl, and downwelling results from positive wind stress curl. Upwelling is sometimes referred to as Ekman suction.

Energetics analysis has been commonly used to reveal regional dynamic mechanisms. It's an effective approach to investigating the variability of a current system [e.g., Lorenz, 1955; Ivchenko et al., 1997; von Storch et al., 2012; Chen et al., 2014; Rieck et al., 2015; Kang et al., 2016; Dong and Zhou, 2022]. In this study, we employ the energetics analysis framework

developed by Kang and Curchitser [2015] to explore the possible mechanism of an anomalous EKE event within the study area.

Following Kang and Curchitser [2015], for a given time-mean state T_0 , the velocity $\mathbf{u} = (u, v)$ is decomposed into its time-mean $\bar{\mathbf{u}}$ and time-varying \mathbf{u}' parts, where $\bar{()}$ and $()'$ represent the time mean and deviation of a variable, respectively. The total density can be expressed as follows:

$$\rho(x, y, z, t) = \rho_r(z) + \rho_a(x, y, z, t), \quad (3)$$

where the reference density ρ_r is the time-mean and spatial-mean density, which is a constant at a given depth z . The perturbation density ρ_a is the difference between the density and reference value. The value $\rho_0 = 1000 \text{ kg m}^{-3}$ is the constant part of ρ_r .

A comparison of selections of the buoyancy frequency N is conducted. The sensitivity test of reference stratification on energetics analysis indicated that the regional constant N at a given depth emphasizes the coastal impacts. Thus, N is defined by

$$N^2 \equiv -\frac{g}{\rho_0} \frac{d\rho_r}{dz}. \quad (4)$$

The Mean Kinetic Energy (MKE), Eddy Kinetic Energy (EKE), Mean Potential Energy (MPE), and Eddy Potential Energy (EPE) are given respectively,

$$\text{MKE} = \frac{1}{2} (\bar{u}^2 + \bar{v}^2), \quad (5)$$

$$\text{EKE} = \frac{1}{2} \overline{(u'^2 + v'^2)}, \quad (6)$$

$$\text{MPE} = \frac{g^2 \bar{\rho}_a^2}{2\rho_0^2 N^2}, \quad (7)$$

$$\text{EPE} = \frac{g^2 \overline{\rho_a'^2}}{2\rho_0^2 N^2}, \quad (8)$$

where \bar{u} and \bar{v} are the means of zonal and meridional velocity components, u' and v' are the anomalies of zonal and meridional velocity components, and g is the gravity constant. To unify the computation, all these energy terms are divided by the density ρ_0 , thus the units of them are m^2s^{-2} (hereafter expressed as cm^2s^{-2}). Kang and Curchitser [2017] evaluated different decompositions of KE, and demonstrated that only with an orthogonal decomposition the physically consistent MKE and EKE could represent the KEs of the mean flow and eddies precisely. Hence, we choose the time-mean state $T_0 = 1$ month in this study in order to examine the seasonal variability of the energy terms. With such definitions, the MKE and EKE represent the monthly averaged KEs of the mean flow (monthly mean flow) and eddies (monthly varying flow), respectively. Physically, they measure the contributions of the actual perturbations that persist longer and shorter than a month, respectively.

The energy conversions between the mean flow and eddies are mainly due to the barotropic instability (i.e., barotropic conversion term, hereafter BT term) and baroclinic instability (i.e., baroclinic conversion term, hereafter BC term and CE term) following Kang and Curchitser [2015]. The conversions can be quantitatively evaluated as follow:

$$\text{MPE} \rightarrow \text{EPE: BC} = -\frac{g^2}{\rho_0^2 N^2} \overline{\rho'_a \mathbf{u}'} \cdot \nabla \overline{\rho_a}, \quad (9)$$

$$\text{EPE} \rightarrow \text{EKE: CE} = -\frac{g}{\rho_0} \overline{\rho'_a w'}, \quad (10)$$

$$\text{MKE} \rightarrow \text{EKE: BT} = -[\overline{u' \mathbf{u}'} \cdot \nabla \bar{u} + \overline{v' \mathbf{u}'} \cdot \nabla \bar{v}], \quad (11)$$

where w is the vertical velocity calculated by the continuity equation based on horizontal velocity u and v . \bar{w} and w' are time-mean and time-varying parts of w . The EKE generation attributes to barotropic and baroclinic instabilities, represented by the conversion terms BT and CE, respectively.

To utilize GLORYS12V1 reanalysis data in the study, data validation is performed before the analysis. The geostrophic eddy kinetic energy (EKE_g) can be derived from sea surface height (SSH) anomalies [Qiu et al., 2018], which are used based on satellite altimetry data:

$$EKE_g = \frac{1}{2} \left[\left(\frac{g}{f} \frac{\partial \eta'}{\partial y} \right)^2 + \left(\frac{g}{f} \frac{\partial \eta'}{\partial x} \right)^2 \right], \quad (12)$$

where g is gravitational acceleration, f is the Coriolis parameter, and η' is the SSH anomalies from the monthly mean.

The time series and spatial patterns of time-mean surface EKE_g are shown in Figure 2. The satellite observation cannot measure sea level beneath sea ice at all, so the time series is the EKE averaged among the area north of south latitude of 65 degrees. The spatially averaged results (Figure 2a) based on satellite altimeter data and reanalysis data exhibit consistent changes with a significant correlation coefficient of 0.95. The spatial distributions also show similar patterns and close magnitudes (Figures 2b and 2c), with relatively high values in the windward of the KP, and the south where the ACC flow through the PET. The results confirm the reliability of the reanalysis data. Moreover, the EKE_g is weak in the coastal area due to the lack of satellite observation, which is unrealistic, and satellite data cannot provide information in the vertical water column. The reanalysis data we used has a more comprehensive imprint for the kinetic energy field of the whole region. Besides, the reanalysis product has a higher spatial resolution to depict the characteristics of eddies.

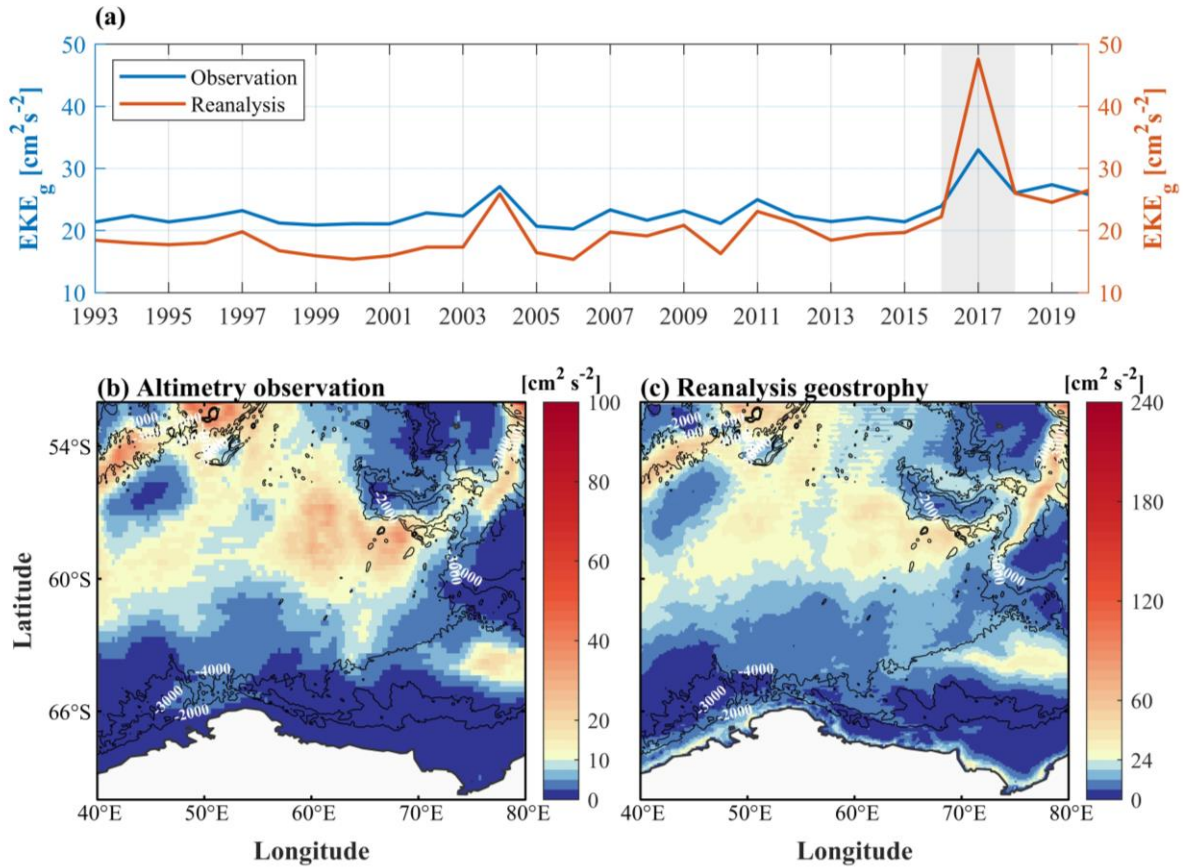


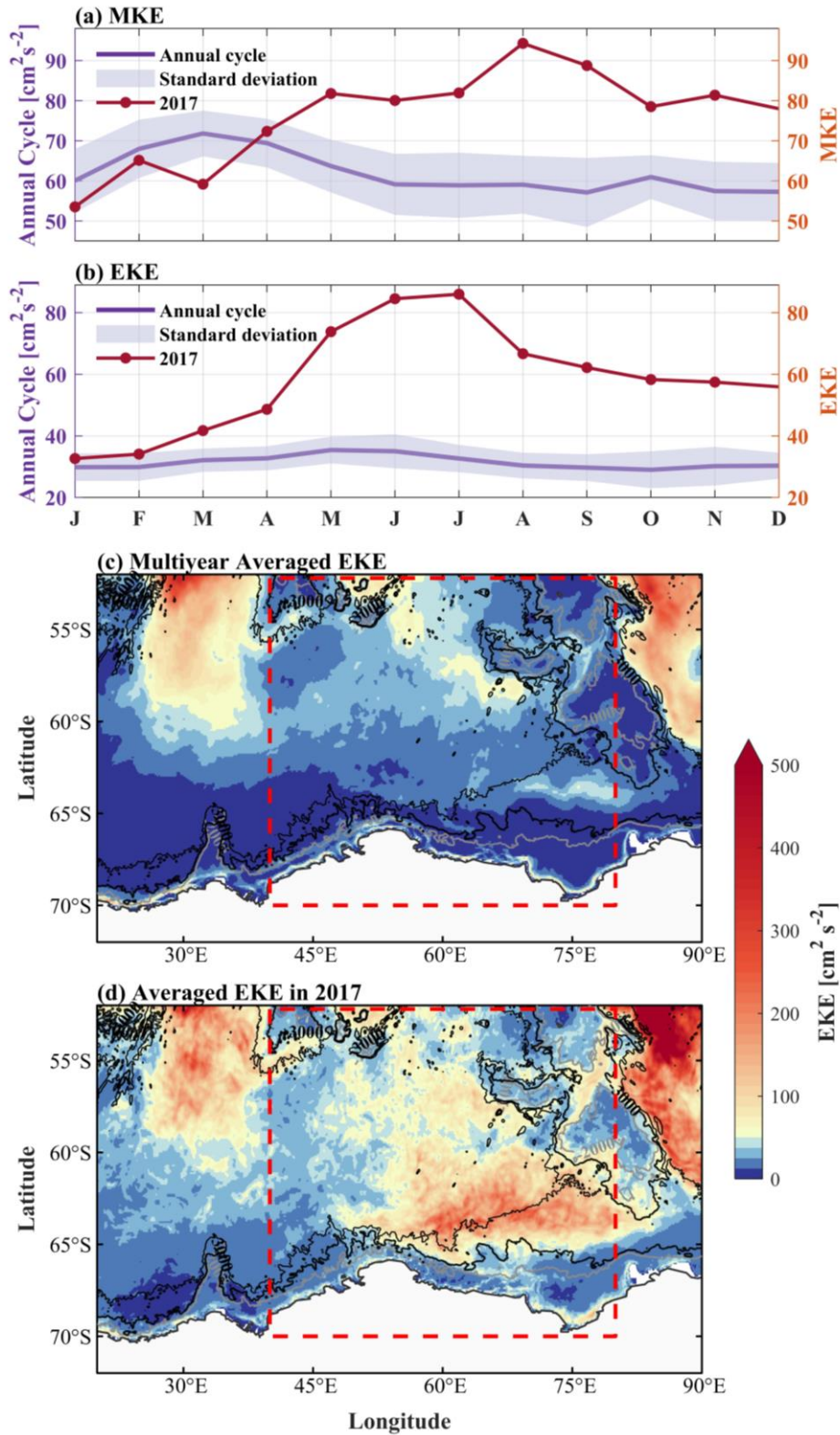
Figure 2. (a) Time series of the yearly area-mean EKE_g (40°-80°E, 52°-65°S), (b) spatial distribution of climatology derived from satellite altimeter data and (c) reanalysis data ($\text{cm}^2 \text{s}^{-2}$).

To describe the ocean dynamics, water mass definition is necessary to analyze the intrusion of warm water. Following Meijers et al. [2010] and Guo et al. [2022], the Circumpolar Deep Water with neutral density variable γ_n (kg m^{-3}) is defined in the thresholds of $28.03 < \gamma_n < 28.27$. The neutral density is calculated from potential temperature and practical salinity. Its anomaly is the difference between monthly neutral density in 2017 compared to the multiyear average between 2010-2020 with the results in 2017 removed in averaging.

3. Results

The sequence of area-mean EKE for 1993-2020 reveals notable interannual variations (Figure 2). It peaks in 2004 and 2017, with the latter year exhibiting a particularly pronounced increase, and indicates an elevated level of variation starting from 2013. The variation is presumed to be influenced by the westerlies and large-scale atmospheric patterns. Notably, the EKE in 2017 reached its peak within the two-decade period. The spatial distribution reveals a prominent pattern in the southwest region of the KP. Annual cycles of surface kinetic energy (MKE and EKE) based on reanalysis data are illustrated in Figure 3. EKE shows less seasonal variation with relatively high values in austral autumn, while MKE is strong in summer. Spring, summer, autumn, and winter used in this study refer to seasons in the southern hemisphere (e.g., the austral summer is December, January, and February). The horizontal distribution of climatology of EKE (Figure 3c) is strongly constrained by regional topography on a large scale. The high values focus on the downstream of plateaus, such as the KP and Crozet islands, and they decrease as the ACC is seasonally weaker in summer.

The seasonal cycles of MKE and EKE suggest distinct anomalies between 2017 and climatology (Figures 3a and 3b). The annual cycle of MKE peaks in March, and is relatively weak in autumn and winter, while in 2017 it increased consistently until August. The annual cycle of EKE is strong in austral autumn. Abnormally, the EKE in 2017 is much higher than in other years. It is significantly anomalous in winter, which is over two times the multiyear average. The surface averaged result of EKE (Figure 3d) shows an unusually high-eddy energy region of 65°-80°E, 60°-65°S, where the ACC flows between Antarctica and the KP.



278 Figure 3. Annual cycle of area-mean surface MKE (a) and EKE (b) for climatology (1993-2020) and
 279 2017 over the region of 40°-80°E, 52°-72°S (units: $\text{cm}^2 \text{s}^{-2}$). (c) Horizontal distribution of multiyear
 280 averaged EKE and in 2017 (d). Dashed red boxes in (c) and (d) indicate the area-mean region. Black
 281 lines mark the 3000-m and 4000-m depth contours from the ETOPO1 bathymetry dataset. The light
 282 grey lines indicate the isobath of 2000 m.

283 The spatial distribution of surface monthly mean EKE of 2017 is illustrated in Figure 4.

284 The distinct high-energy eddies appeared in the southwest region of the KP ($\sim 66^{\circ}45' S$)

285 from April. It seems to propagate from east to west in austral winter, lasting until the next

286 year. Moreover, the anomalous strong EKE exists from the surface to the deep layer, shown

287 as in Figure 5a. The three-dimensional (longitude-latitude-depth) structure of EKE reflects

288 the strong eddy activities in both surface and deep layers. EKEs at different depths exhibit

289 high values in the anomalous region. Comparing the meridional (latitude-depth) transects of

290 monthly MKE and mean EKE between the anomaly year (2017) and multiyear average

291 (Figures 5b-5e), the anomalies of kinetic energy in 2017 are prominent. High values of MKE

292 are observed in the Fawn Trough and the south side of the KP. Strong anomalies of EKE and

293 MKE are both distinct on the south side, nearly $64^{\circ}S$ (Figures 5b and 5c).

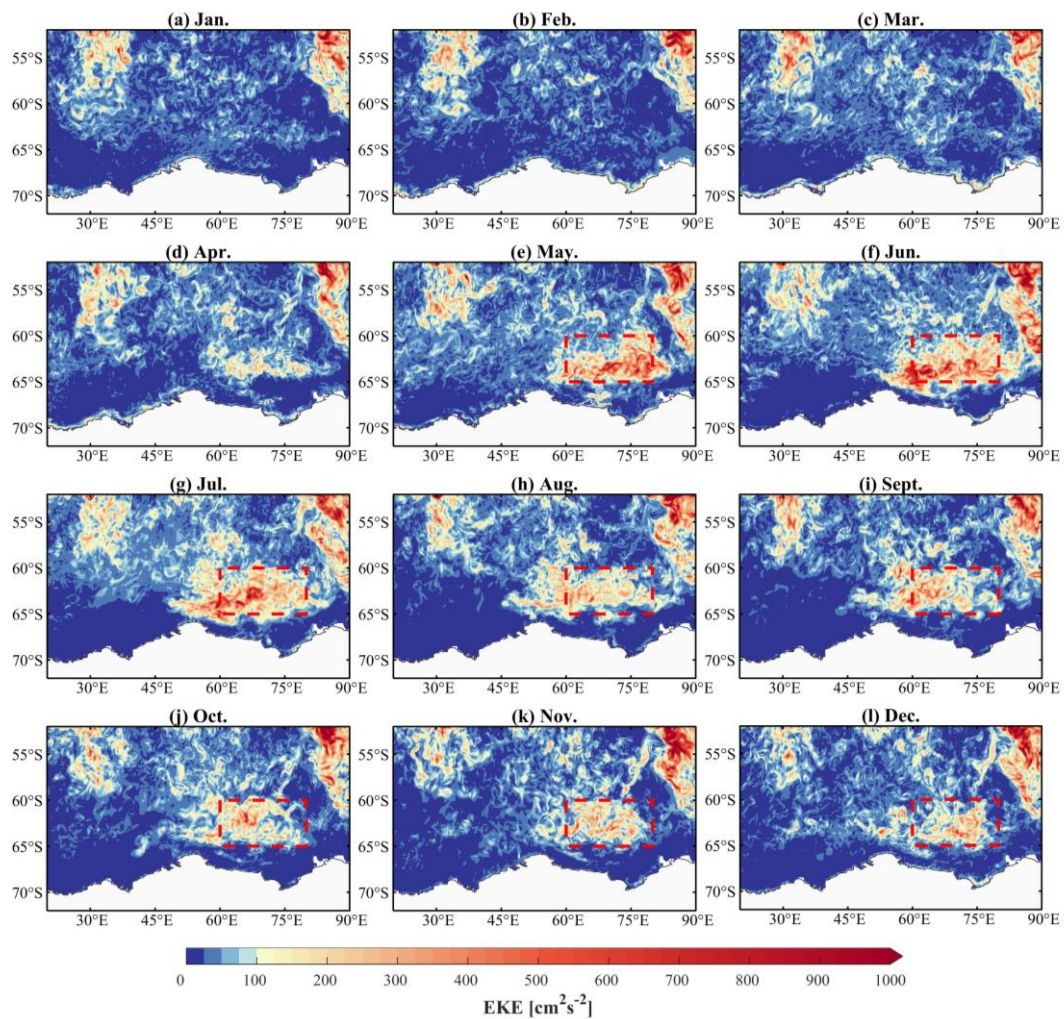


Figure 4. Spatial distribution of monthly mean surface EKE ($\text{cm}^2 \text{s}^{-2}$) in 2017. (a-l) show January to December. The mainly anomalous EKE region focused on is indicated by the dashed red box (60° - 80°E , 60° - 65°S).

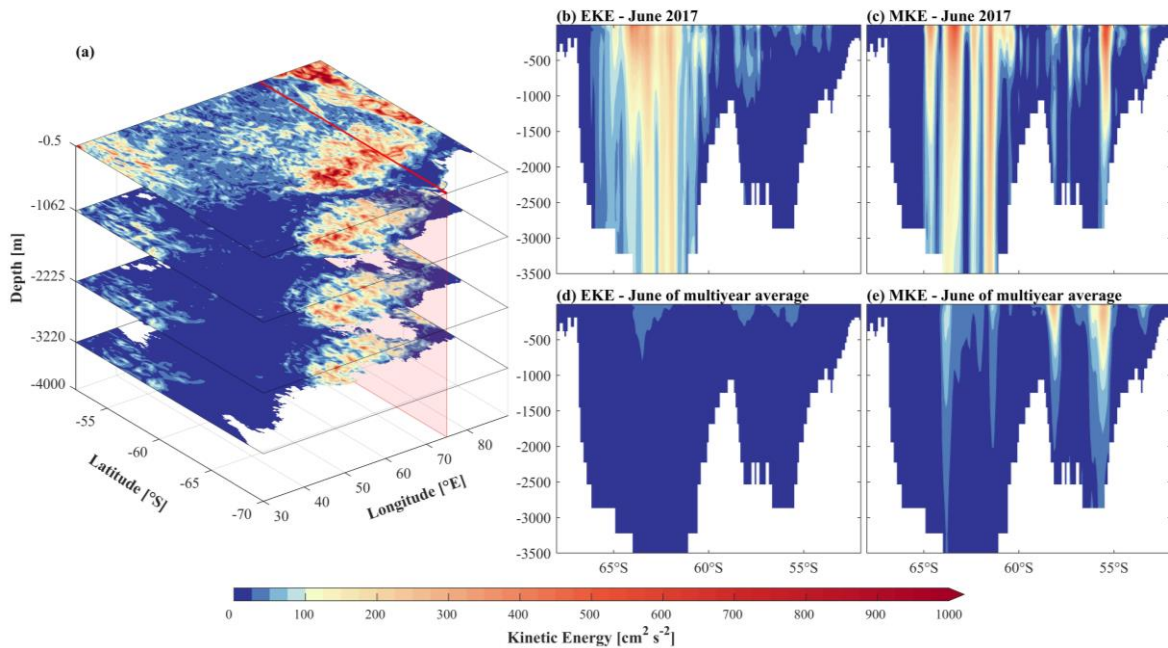


Figure 5. (a) Three-dimensional (longitude-latitude-depth) structure of EKE ($\text{cm}^2 \text{s}^{-2}$) in June 2017, when the integrated EKE in the anomalous region was the strongest in the event. The latitude-depth transects are the 75°E of MKE (b and c) and mean EKE (d and e) in June of 2017 and the multiyear average (denoted by the red transect in (a)).

Previous studies have highlighted the importance of barotropic and baroclinic instabilities as the primary sources of EKE. Energetics analysis is performed to investigate the energy conversion processes contributing to the EKE growth in the selected anomaly region, denoted by the dashed red boxes in Figure 4. Monthly averaged area-mean of MKE, EKE, and Eddy Potential Energy (EPE) in the anomaly region are considered (Figure 6a), with these results representing the integrated densities within the upper 500 meters of the water column. The EKE growth was initiated in March and peaked in June, following the peak of EPE in April. In June and August, MKE exhibited high values, indicating strong kinetic energy during the winter. Their spatial distributions from April to July are shown in

Figure 7. The kinetic energy (EKE and MKE) was strong in winter, demonstrating the dominance of kinetic energy, while the EPE weakened after May.

To further analyze the contributions to EKE growth, the depth-integrated energy conversion rate densities (upper 500 m) are calculated, based on Equations 9-11 as described in the methods. All peaks of energy conversion (BC: MPE \rightarrow EPE, CE: EPE \rightarrow EKE, and BT: MKE \rightarrow EKE) are observed in May (Figure 6b), preceding the strongest EKE anomaly (Figure 6a). 60°-80°E averaged depth-integrated energy conversion rate densities are illustrated in Figure 8. Baroclinic energy conversions (BC and CE) exhibit positive values (Figures 8a and 8b). It is observed that strong baroclinic conversion occurred starting from April, with values exceeding $5 \times 10^{-8} \text{ m}^2 \text{ s}^{-3}$. Both BC and CE propagated southward over a distance of about 1.5° ($\sim 170 \text{ km}$) from April to November, while the barotropic energy conversion (BT) shows negative values with southward propagation (Figure 8c).

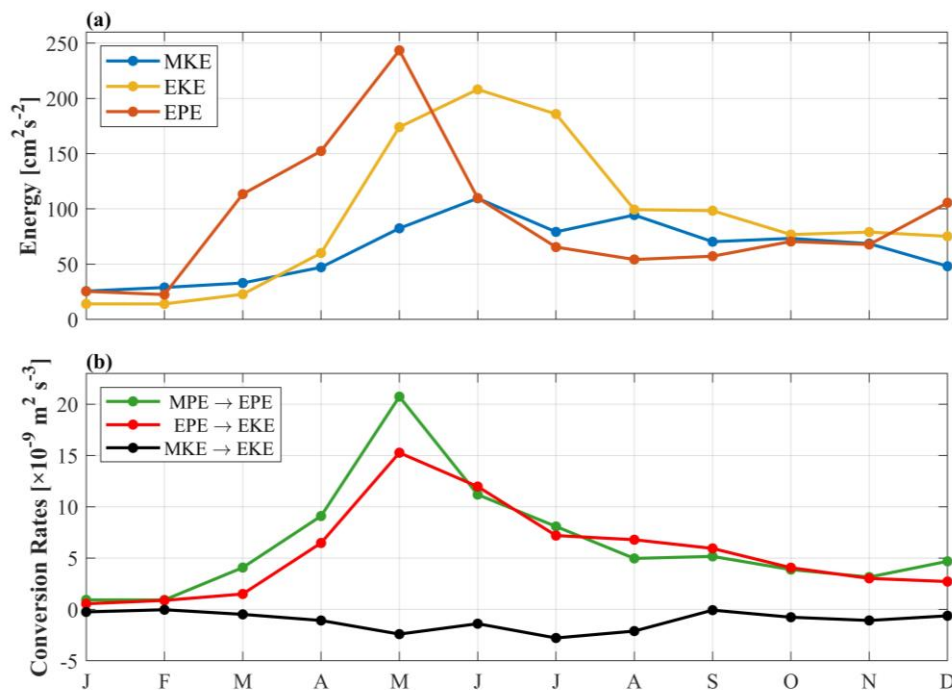
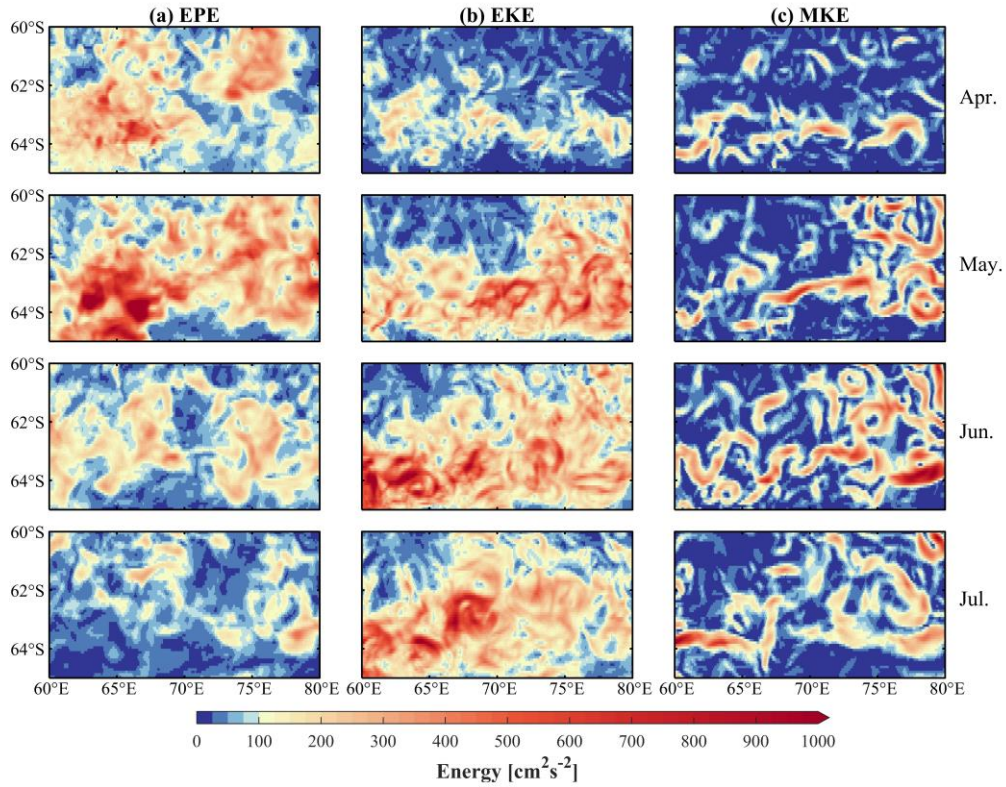


Figure 6. Time series of monthly mean depth-integrated (upper 500 m) energy densities (MKE, EKE, and EPE, unit: $\text{cm}^2 \text{ s}^{-2}$) (a) and energy conversion rate densities (unit: $\text{m}^2 \text{ s}^{-3}$) (b) averaged over the selected subregion in 2017, the dashed red box indicated in Figure 4.



327 Figure 7. Spatial distribution of upper 500 m integrated EPE (a), EKE (b), and MKE (c) densities
 328 (unit: $\text{cm}^2 \text{s}^{-2}$) in the subregion from April to July in 2017.

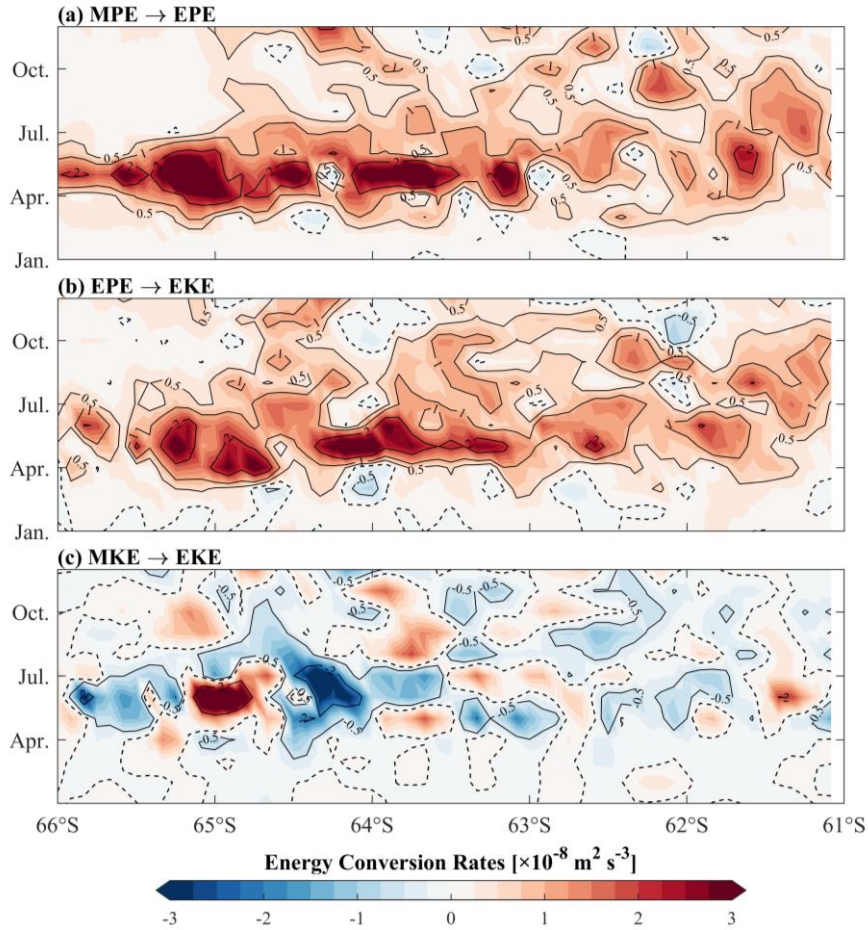


Figure 8. Hovmöller diagrams of 60°-80°E averaged upper 500-m integrated energy conversion rate density (unit: $\text{m}^2 \text{s}^{-3}$) in Equation 9-11 in 2017, (a) BC: MPE \rightarrow EPE, (b) CE: EPE \rightarrow EKE, and (c) BT: MKE \rightarrow EKE.

According to the results of three-dimensional EKE in Figure 5, it is evident that EKE remains robust in the deeper ocean, experiencing minimal weakening in comparison to the surface. Our investigation encompasses energetics analysis across all ocean layers. Vertical profiles of averaged energy and energy conversion rates for all layers during May 2017 are provided in Figure 9. Both MKE and EKE exhibit similar patterns with relatively less variation from the surface to the deep layers, whereas EPE shows a peak at the surface, followed by a decline within the upper 50 meters, and then a rapid increase in the upper 1000 m (Figure 9a). This pattern is similar to the energy conversion of MPE to EPE (Figure 9b). EPE and the baroclinic conversion of MPE to EPE, as well as EPE to EKE, exhibit particularly notable intensities within the depth range of the Circumpolar Deep Water (CDW), approximately between 500 and 2000 meters.

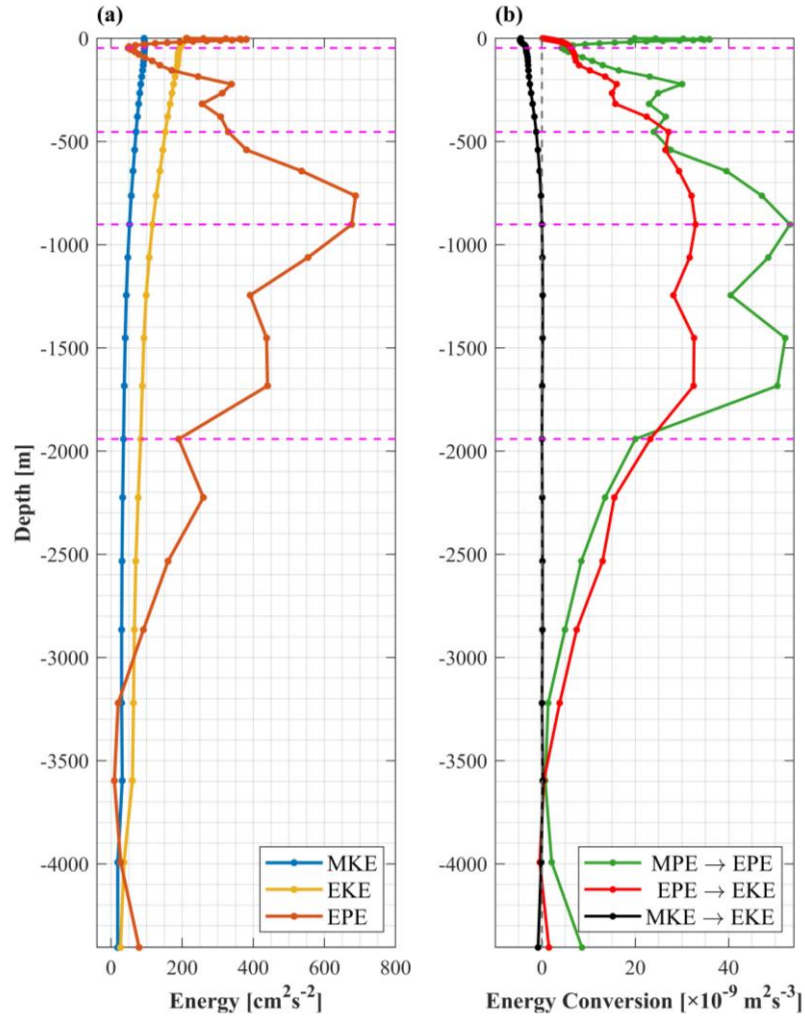


Figure 9. Vertical profile of energy (a) and energy conversion (b) averaged over the subregion (60°-80°E, 60°-65°S) in May 2017 (unit: $\text{m}^2 \text{s}^{-3}$). Four typical layers are indicated by the dashed magenta lines at depths near 50 m, 500 m, 1000 m, and 2000 m, respectively.

To explore the underlying mechanisms of anomalous EKE variability, the isopycnals of neutral density within the upper 2000 m, along with their anomalies compared to multiyear averages are illustrated in Figure 10, where the baroclinic energy conversions were distinct (Figure 9b). The first isopycnal near the surface indicates the upper boundary of the CDW. Isopycnals in the southwest sector of the KP deviated considerably from the climatological values, indicated by the black and magenta curves (the left panels in Figure 10). The neutral densities show significantly positive anomalies in the coastal region (the right panels in

Figure 10), particularly during the period of most pronounced baroclinic energy conversion in May exhibited in Figures 6b, 8a, and 8b.

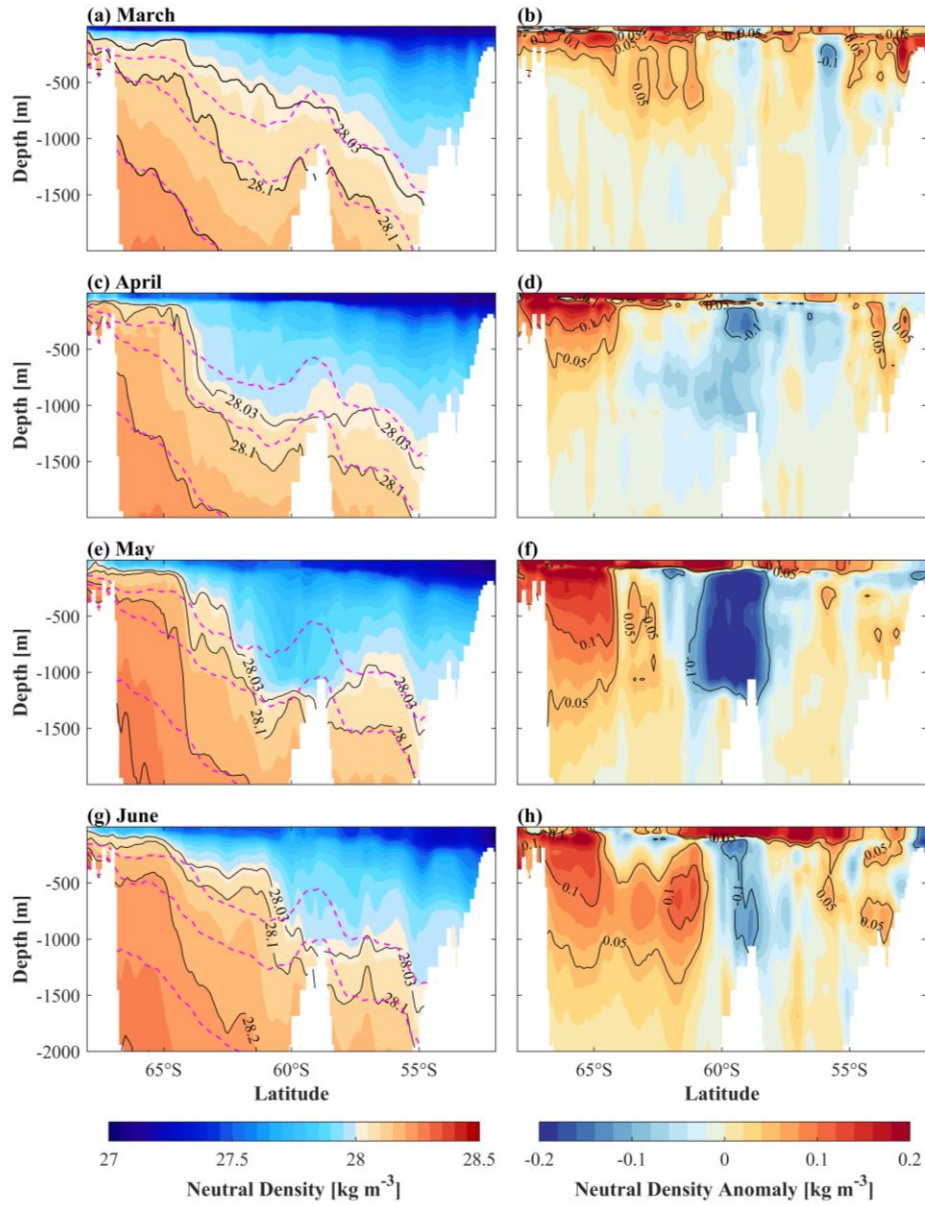
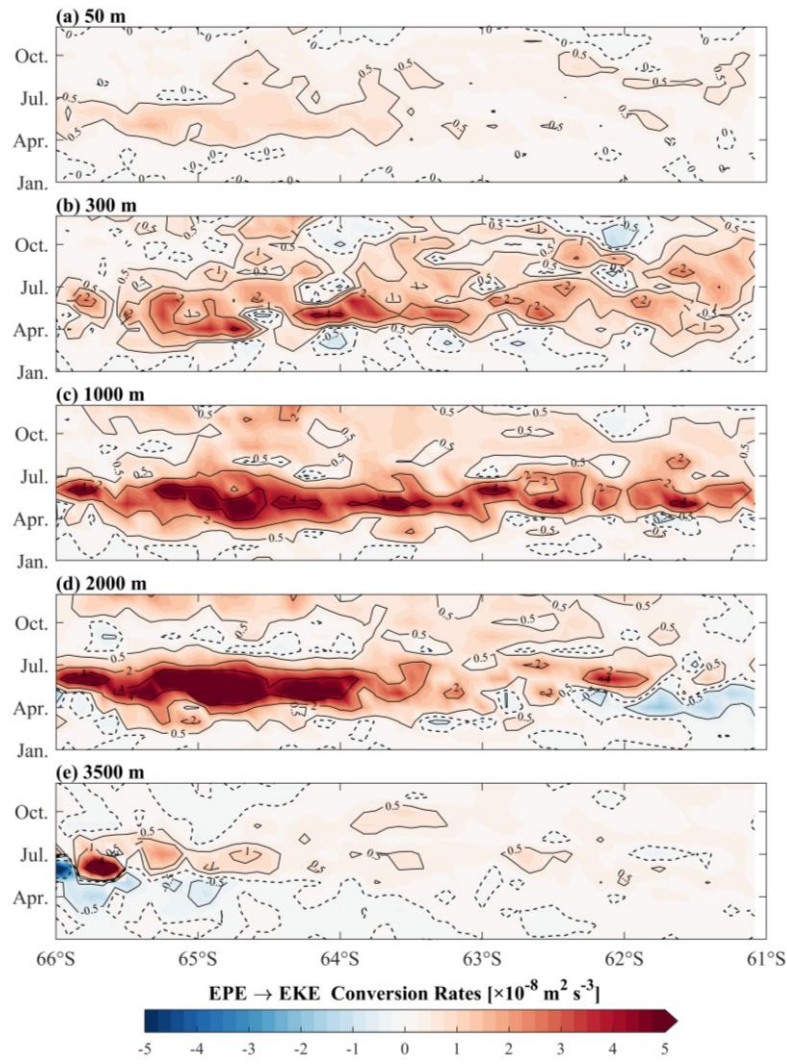


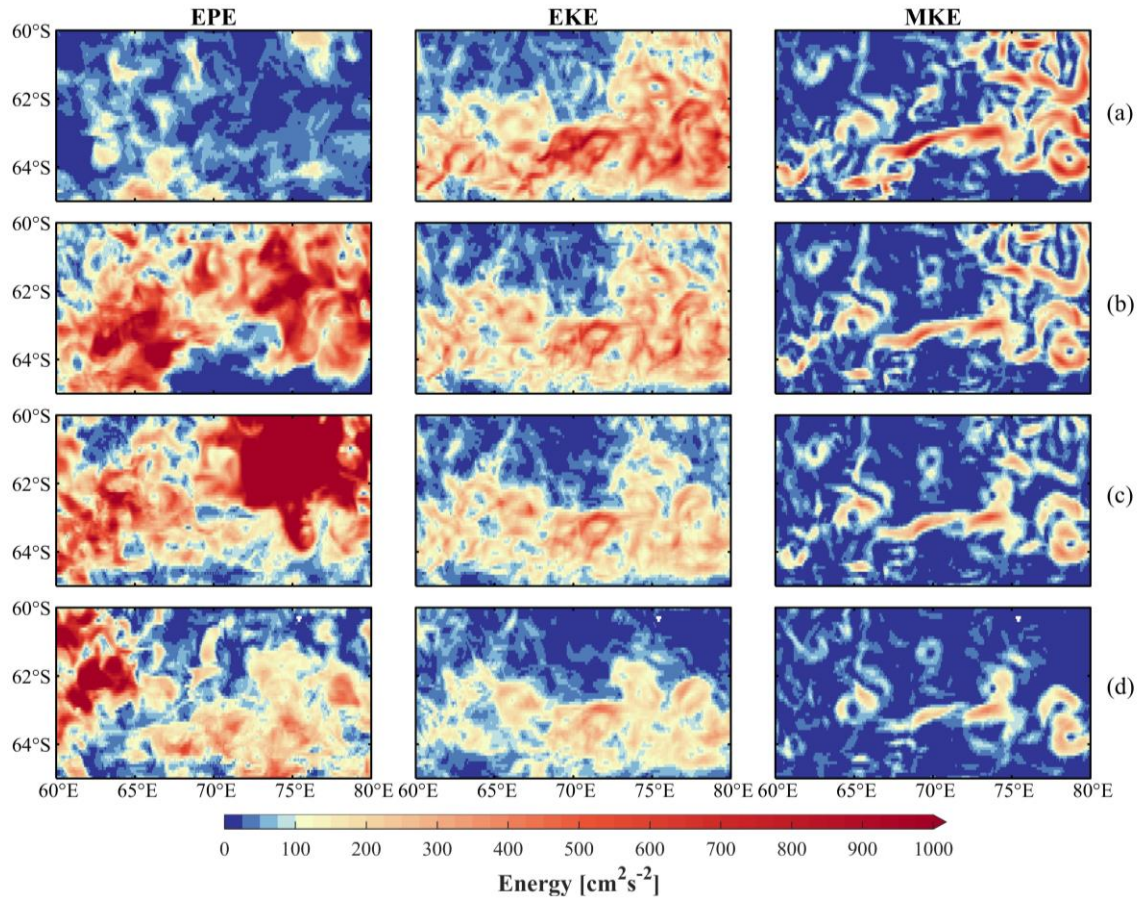
Figure 10. The latitude-depth transects of neutral density (γ_n , kg m^{-3}) and its anomaly at 75°E in March (a and b), April (c and d), May (e and f), and June (g and h) in 2017. The black curves represent isopycnals of neutral density in 2017 for the transects, and the magenta curves represent the multiyear average of 2010-2020. The isopycnals of 28.03 kg m^{-3} indicate the upper boundary of the CDW.

The meridionally integrated averages of CE (baroclinic energy conversion of $EPE \rightarrow EKE$) in different layers are shown in Figure 11. CE is comparatively weak in the surface layer, and it diminishes below the approximate depth of 2000 m (Figure 11e), transitioning from strong positive values. Moreover, the active baroclinic conversion is associated with the robust EKE anomaly during the period spanning from April to July across all depths. Similar patterns are reflected in the horizontal distribution of energy, as illustrated in Figure 12. Both the MKE and EKE extend consistently throughout the water column displaying minimal fluctuations (the middle and right panels in Figure 12). In contrast, EPE experiences notable enhancement within the depth range of the CDW, as shown in the first column of Figures 12b and 12c, indicating its greater concentration in this area.



376

377 Figure 11. Hovmöller diagrams of baroclinic energy conversion rates (unit: $\text{m}^2 \text{s}^{-3}$) of EPE to EKE
 378 (the CE term in Equation 10), which are 60°-80°E integral averages of different layers in 2017, near
 379 50 m, 300 m, 1000 m, 2000 m, and 3500 m, respectively.



381 Figure 12. Horizontal distribution of EPE, EKE, and MKE (unit: $\text{cm}^2 \text{s}^{-2}$) in four typical layers (a-d) in
 382 May 2017, as Figure 10 shows, which are indicated by the dashed magenta lines at depths near 50 m,
 383 500 m, 1000 m, and 2000 m, respectively.

384

385 Moreover, $65^\circ\text{-}80^\circ\text{E}$ meridional averaged monthly wind-induced Ekman pumping
 386 velocities W_{ek} in the region between $60^\circ\text{-}72^\circ\text{S}$ in March-May are depicted in Figure 13. The
 387 results in 2017 show obvious positive anomalies compared with the multiyear average
 388 (Figure 13a). The monthly Ekman pumping velocity in 70°S , denoted by the dashed grey line
 389 in Figure 13a, is shown in Figure 13b. There are two distinct peaks in April and October, with
 390 the former one having impacts on the anomalous event.

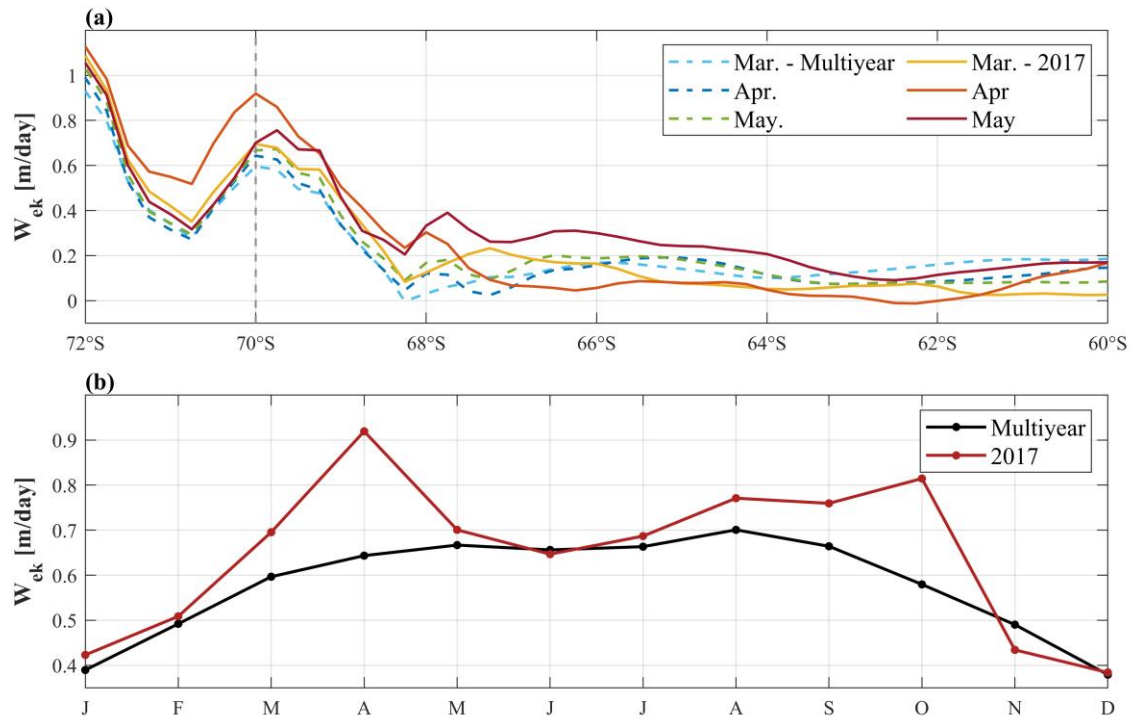


Figure 13. (a) 65°-80°E meridionally averaged monthly Ekman pumping velocity W_{ek} (m s^{-1} , positive: upward) in the region between 60°-72°S in March-May. (b) Meridional averaged Ekman pumping velocity W_{ek} in 70°S of multiyear mean and 2017, denoted by the dashed grey line in (a).

4. Discussion

4.1. Primary Energy Source for the EKE Anomaly Event

Based on the energetics analysis, energy conversions correspond well with the variations of eddy energy, and the responses of EKE show a time lag after a substantial buildup of potential energy (Figures 6 and 7). Baroclinic energy conversions (BC and CE) exhibit positive values before the emergence of the EKE anomaly, representing their contributions to the anomalous EKE. It is implied that Mean Potential Energy (MPE) delivers energy into eddies, resulting in the enhancement of EPE. Subsequently, EKE receives energy from EPE, while barotropic conversion contributes to the reduction of EKE.

While the ACC is well-known for its contribution of energy to the subpolar region through barotropic conversion, our analysis within the specific study region reveals an inverse conversion pattern with negative barotropic conversion (BT in Figures 6b and 8c). The regional energy cascade operates differently compared to the broader ACC. Here, it's the baroclinic conversion that predominantly influences the energy input, involving the conversion from available potential energy to kinetic energy through baroclinic processes, instead of barotropic energy conversion contributing to the energy input. Furthermore, the negative southward propagation of the BT highlights that the barotropic conversion influences the mean flow after strong energy disturbances. These interactions between eddies and the mean flow result in distinct energy conversion patterns. Consequently, the pronounced anomalous EKE observed during the winter months can be attributed to robust baroclinic energy conversion, making it the primary factor driving the enhancement of EKE in this specific region.

4.2. Possible Mechanisms for the Strong Baroclinic Energy Conversion

In the southwest region of the KP, there is a notable steepening of isopycnals from March 2017 (Figure 10b), particularly during May when baroclinic energy conversion is most pronounced (Figures 6b, 8a, and 8b). The flattening of isopycnals is demonstrated to indicate the release of potential energy and the occurrence of baroclinic instability [Rintoul, 2018; Cai et al., 2022]. The anomalies observed in isopycnals lead to vigorous baroclinic instability, which aligns remarkably with the period of notable baroclinic energy conversion from EPE to EKE (CE, Figure 11). The energy input to EKE is concentrated within the depth range of the CDW, corresponding with the vertical distribution depicted in Figure 9b (denoted by the red line).

The intrusion of anomalous warm CDW plays a pivotal role in steepening the isopycnals, particularly in the anomalous region. Consequently, Baroclinic instability is initiated,

accompanied by the restoration of isopycnals, where the baroclinic pathway originates. This intensified baroclinic instability facilitated the conversion from MPE to EPE, subsequently culminating in the generation of EKE. As a result, the patterns of EKE exhibit intensely positive anomalies at the surface layer and in the internal ocean.

4.3. Impacts of Wind Changes

Another pronounced phenomenon is that the depth of the upper boundary of the CDW is distinctly shallower than the normal situation, as indicated by the isopycnal of 28.03 kg m^{-3} in Figure 10. Previous studies have proposed that the CDW intrusion into Prydz Bay (PB) during austral autumn and winter is significantly influenced by the wind patterns north of the shelf break from January to May [e.g., Guo et al., 2022]. During the summer of 2017, unusual wind patterns were suggested to have occurred in PB, which even resulted in strong advection of warmer waters towards the shelf region in January [Meehl et al., 2019; Wang et al., 2019; Sabu et al., 2021]. In the present study, changes in the wind field during the period are revealed to strengthen regional Ekman divergence, leading to anomalous strong Ekman pumping, particularly in the southern coastal area (Figure 13a). The wind-induced Ekman pumping velocities from March to May in the anomaly region significantly exceeded the multiyear average (Figure 13b), further promoting the upwelling of CDW. That facilitated the development of meridional density gradients, amplifying the lifting of isopycnals near the coast. Consequently, the baroclinic energy conversion was intensified, ultimately resulting in the observed anomalies in EKE. In summary, these processes contributed to the heightened generation of eddies and enhancement of eddy energy of the system.

Collectively, our findings contribute significantly to the understanding of energy dynamics and transformation mechanisms in the region. Previous studies predominantly focused on the baroclinic instability induced by wind forcing [e.g., Wu et al., 2017; Matsuta and Masumoto, 2023], while this study emphasizes the important role played by currents in

the interior ocean. Despite other Antarctic regions also experienced positive anomalies in spatially averaged EKE during the same year, they did not exhibit distinctive phenomena observed in our study area. We speculate that the variations in EKE may be influenced by large-scale climate modes, and these differences could be attributed to the combined effects of ocean currents, topography, and other unique characteristics specific to our study region. Future research endeavors could further explore the feedback mechanisms operating in polar regions.

5. Conclusions

In this study, a systematic energetics analysis framework is employed to examine the notable anomalies of an intensified EKE event observed in the southwest region of the Kerguelen Plateau in 2017 based on a reanalysis product. The EKE anomaly existing at all depths emerges in April, reaches its peak during the austral winter, and persists into the following summer. Our results indicate that the anomalously high-intensity EKE during this period predominantly results from baroclinic instability, with its primary source being the available potential energy. Potential mechanisms have been proposed to elucidate the processes occurring in both the upper and deeper ocean layers, and we emphasized the energetics dynamics at depth. The intrusion of anomalous warm Circumpolar Deep Water intensifies the baroclinic energy conversion, which contributes to the EKE anomalies. And anomalous strong wind-induced Ekman pumping serves to amplify the lifting of isopycnals, which also intensifies the baroclinic instability. Thus, the powerful baroclinic energy pathway ultimately results in a substantial increase in regional EKE. Our study sheds new light on the underlying mechanisms governing local polar dynamics and provides insights into the intricate interaction between ocean dynamics and energy distribution in the Antarctic.

479 We have analyzed the underlying mechanisms of eddy dynamics, and a possible physical
480 process of EKE responding to changes in wind patterns is proposed. It is important to note
481 that we have primarily focused on the oceanic domain. The intrusion of warm CDW in the
482 ocean interior is emphasized to be the primary factor leading to the strong anomalies in EKE.
483 Further investigations would be necessary to explore how regional mesoscale eddy fields
484 respond to large-scale atmospheric patterns, and if these patterns have impacts on the
485 intrusion of CDW. We call for high-resolution air-sea coupled models in the subpolar region
486 to gain a more comprehensive understanding of regional dynamics and their ecological
487 implications in the Antarctic.

488

Acknowledgments

This work is funded by the Shanghai Frontiers Science Center of Polar Research. The authors have no conflicts of interest with these data.

Data Availability Statement

The reanalysis product GLORYS12V1 (GLOBAL_REANALYSIS_PHY_001_030) is provided by Copernicus Marine Environmental Monitoring Service (CMEMS, https://data.marine.copernicus.eu/product/GLOBAL_MULTIYEAR_PHY_001_030/download). Altimeter satellite gridded data (SEALEVEL_GLO_PHY_L4_MY_008_047) is available from CMEMS (https://data.marine.copernicus.eu/product/SEALEVEL_GLO_PHY_L4_MY_008_047/download). Wind data is obtained from the European Centre for Medium-Range Weather Forecasts (ECMWF) Reanalysis Version 5 (ERA5) dataset (<https://cds.climate.copernicus.eu/>). The bathymetry can be found at <https://www.ncei.noaa.gov/products/etopo-global-relief-model>.

503 **References**

- 504 Bestley, S., E. van Wijk, M. Rosenberg, R. Eriksen, S. Corney, K. Tattersall,
505 and S. Rintoul (2020), Ocean circulation and frontal structure near the southern
506 Kerguelen Plateau: The physical context for the Kerguelen Axis ecosystem
507 study, *Deep-Sea Research Part II-Topical Studies in Oceanography*, 174,
508 doi:10.1016/j.dsr2.2018.07.013.
- 509 Cai, Y., D. Chen, M. R. Mazloff, T. Lian, and X. Liu (2022), Topographic
510 modulation of the wind stress impact on eddy activity in the Southern Ocean,
511 *Geophysical Research Letters*, 49(13), doi:10.1029/2022gl097859.
- 512 Chen, R., G. R. Flierl, and C. Wunsch (2014), A description of local and
513 nonlocal eddy-mean flow interaction in a Global Eddy-Permitting State
514 Estimate, *Journal of Physical Oceanography*, 44(9), 2336-2352,
515 doi:10.1175/jpo-d-14-0009.1.
- 516 Dong, H., and M. Zhou (2022), Dynamical controls of the eastward transport of
517 overwintering *Calanus finmarchicus* from the Lofoten Basin to the continental
518 slope, *Journal of Geophysical Research: Oceans*, doi:10.1029/2022JC018909.
- 519 Foldvik, A., and T. Gammelsrod (1988), Notes on Southern Ocean
520 hydrography, sea-ice and bottom water formation, *Palaeogeography*
521 *Palaeoclimatology Palaeoecology*, 67(1-2), 3-17, doi:10.1016/0031-
522 0182(88)90119-8.
- 523 Frenger, I., M. Muennich, N. Gruber, and R. Knutti (2015), Southern Ocean
524 eddy phenomenology, *Journal of Geophysical Research-Oceans*, 120(11),
525 7413-7449, doi:10.1002/2015jc011047.
- 526 Fu, G., Y. Yang, X. S. Liang, and Y. Zhao (2023), Characteristics and dynamics
527 of the interannual eddy kinetic energy variation in the central Pacific sector of
528 the Southern Ocean, *Journal of Geophysical Research: Oceans*, 128(10),
529 doi:10.1029/2022jc019618.
- 530 Fu, L.-L., D. B. Chelton, P.-Y. Le Traon, and R. Morrow (2010), Eddy
531 dynamics from satellite altimetry, *Oceanography*, 23(4), 14-25,
532 doi:10.5670/oceanog.2010.02.
- 533 Gille, S. T. (1994), Mean sea-surface height of the Antarctic Circumpolar
534 Current from Geosat data: Method and application, *Journal of Geophysical*
535 *Research-Oceans*, 99(C9), 18255-18273, doi:10.1029/94jc01172.
- 536 Guo, G., L. Gao, J. Shi, and Y. Zu (2022), Wind-driven seasonal intrusion of
537 modified Circumpolar Deep Water onto the continental shelf in Prydz Bay, East
538 Antarctica, *Journal of Geophysical Research: Oceans*, 127(12),
539 doi:10.1029/2022jc018741.

540 Heywood, K. J., M. D. Sparrow, J. Brown, and R. R. Dickson (1999), Frontal
 541 structure and Antarctic Bottom Water flow through the Princess Elizabeth
 542 Trough, Antarctica, *Deep-Sea Research Part I-Oceanographic Research*
 543 *Papers*, 46(7), 1181-1200, doi:10.1016/s0967-0637(98)00108-3.

544 Hogg, A. M., M. P. Meredith, D. P. Chambers, E. P. Abrahamson, C. W.
 545 Hughes, and A. K. Morrison (2015), Recent trends in the Southern Ocean eddy
 546 field, *Journal of Geophysical Research: Oceans*, 120(1), 257-267,
 547 doi:10.1002/2014jc010470.

548 Hogg, A. M., T. Penduff, S. E. Close, W. K. Dewar, N. C. Constantinou, and J.
 549 Martinez-Moreno (2022), Circumpolar variations in the chaotic nature of
 550 Southern Ocean eddy dynamics, *Journal of Geophysical Research-Oceans*,
 551 127(5), doi:10.1029/2022jc018440.

552 Hughes, C. W., and E. R. Ash (2001), Eddy Forcing of the mean flow in the
 553 Southern Ocean, *Journal of Geophysical Research-Oceans*, 106(C2), 2713-
 554 2722, doi:10.1029/1999jc900332.

555 Ivchenko, V. O., A. M. Treguier, and S. E. Best (1997), A kinetic energy budget
 556 and internal instabilities in the Fine Resolution Antarctic Model, *Journal of*
 557 *Physical Oceanography*, 27(1), 5-22, doi:10.1175/1520-
 558 0485(1997)027<0005:Akebai>2.0.Co;2.

559 Kang, D., and E. N. Curchitser (2015), Energetics of eddy-mean flow
 560 interactions in the Gulf Stream region, *Journal of Physical Oceanography*,
 561 45(4), 1103-1120, doi:10.1175/jpo-d-14-0200.1.

562 Kang, D., and E. N. Curchitser (2017), On the evaluation of seasonal variability
 563 of the ocean kinetic energy, *Journal of Physical Oceanography*, 47(7), 1675-
 564 1683, doi:10.1175/jpo-d-17-0063.1.

565 Kang, D., E. N. Curchitser, and A. Rosati (2016), Seasonal variability of the
 566 Gulf Stream kinetic energy, *Journal of Physical Oceanography*, 46(4), 1189-
 567 1207, doi:10.1175/jpo-d-15-0235.1.

568 Liu, C., Z. Wang, C. Cheng, R. Xia, B. Li, and Z. Xie (2017), Modeling
 569 modified Circumpolar Deep Water intrusions onto the Prydz Bay continental
 570 shelf, East Antarctica, *Journal of Geophysical Research: Oceans*, 122(7), 5198-
 571 5217, doi:10.1002/2016jc012336.

572 Lorenz, E. N. J. T. A. (1955), Available potential energy and the maintenance of
 573 the general circulation, 7, 157-167.

574 Martinez-Moreno, J., A. M. Hogg, and M. H. England (2022), Climatology,
 575 seasonality, and trends of spatially coherent ocean eddies, *Journal of*
 576 *Geophysical Research-Oceans*, 127(7), doi:10.1029/2021jc017453.

577 Martinez-Moreno, J., A. M. Hogg, A. E. Kiss, N. C. Constantinou, and A. K.
 578 Morrison (2019), Kinetic energy of eddy-like features from sea surface

579 altimetry, *Journal of Advances in Modeling Earth Systems*, 11(10), 3090-3105,
580 doi:10.1029/2019ms001769.

581 Matsuta, T., and Y. Masumoto (2023), Energetics of the Antarctic Circumpolar
582 Current. Part I: The Lorenz energy cycle and the vertical energy redistribution,
583 *Journal of Physical Oceanography*, 53(6), 1467-1484, doi:10.1175/jpo-d-22-
584 0133.1.

585 Meehl, G. A., J. M. Arblaster, C. T. Y. Chung, M. M. Holland, A. DuVivier, L.
586 Thompson, D. Yang, and C. M. Bitz (2019), Sustained ocean changes
587 contributed to sudden Antarctic sea ice retreat in late 2016, *Nature*
588 *Communications*, 10, doi:10.1038/s41467-018-07865-9.

589 Meijers, A. J. S., A. Klocker, N. L. Bindoff, G. D. Williams, and S. J. Marsland
590 (2010), The circulation and water masses of the Antarctic shelf and continental
591 slope between 30 and, *Deep Sea Research Part II: Topical Studies in*
592 *Oceanography*, 57(9-10), 723-737, doi:10.1016/j.dsr2.2009.04.019.

593 Meredith, M. P., and A. M. Hogg (2006), Circumpolar response of Southern
594 Ocean eddy activity to a change in the Southern Annular Mode, *Geophysical*
595 *Research Letters*, 33(16), doi:10.1029/2006gl026499.

596 Morrow, R., R. Coleman, J. Church, and D. Chelton (1994), Surface eddy
597 momentum flux and velocity variances in the Southern Ocean from Geosat
598 altimetry, *Journal of Physical Oceanography*, 24(10), 2050-2071,
599 doi:10.1175/1520-0485(1994)024<2050:Semfav>2.0.Co;2.

600 Morrow, R., M. L. Ward, A. M. Hogg, and S. Pasquet (2010), Eddy response to
601 Southern Ocean climate modes, *Journal of Geophysical Research-Oceans*, 115,
602 doi:10.1029/2009jc005894.

603 Mou, W., G. Yang, Q. Hao, Z. Xu, and C. Li (2021), The zooplankton
604 community in Cosmonaut Sea: Community structure and environmental factors,
605 *Oceanologia et Limnologia Sinica*, 52(4), 925-935.

606 Nunes Vaz, R. A., and G. W. Lennon (1996), Physical oceanography of the
607 Prydz Bay region of Antarctic waters, *Deep-Sea Research Part I:*
608 *Oceanographic Research Papers*, 43(5), 603-641, doi:10.1016/0967-
609 0637(96)00028-3.

610 Orsi, A., W. Thomas, and W. D. Nowlin (1995), On the meridional extent and
611 fronts of the Antarctic Circumpolar Current.pdf, *Deep Sea Research Part I:*
612 *Oceanographic Research Papers*.

613 Qiu, B., S. Chen, P. Klein, J. Wang, H. Torres, L.-L. Fu, and D. Menemenlis
614 (2018), Seasonality in Transition Scale from Balanced to Unbalanced Motions
615 in the World Ocean, *Journal of Physical Oceanography*, 48(3), 591-605,
616 doi:10.1175/jpo-d-17-0169.1.

617 Rieck, J. K., C. W. Boning, R. J. Greatbatch, and M. Scheinert (2015), Seasonal
618 variability of eddy kinetic energy in a global high-resolution ocean model,
619 *Geophysical Research Letters*, 42(21), 9379-9386, doi:10.1002/2015gl066152.

620 Rintoul, S. R. (2018), The global influence of localized dynamics in the
621 Southern Ocean, *Nature*, 558(7709), 209-218, doi:10.1038/s41586-018-0182-3.

622 Rosso, I., A. M. Hogg, A. E. Kiss, and B. Gayen (2015), Topographic influence
623 on submesoscale dynamics in the Southern Ocean, *Geophysical Research*
624 *Letters*, 42(4), 1139-1147, doi:10.1002/2014gl062720.

625 Sabu, P., M. P. Subeesh, K. K. Sivakrishnan, and N. Anilkumar (2021), Causes
626 and impacts of anomalous warming in the Prydz Bay, East Antarctica during
627 austral summer 2016-17, *Polar Science*, 30, doi:10.1016/j.polar.2021.100660.

628 Shi, F., Y. Luo, R. Wu, Q. Yang, R. Chen, C. Wang, Y. Lin, and D. Chen
629 (2023), Contrasting trends in short-lived and long-lived mesoscale eddies in the
630 Southern Ocean since the 1990s, *Environmental Research Letters*, 18(3),
631 doi:10.1088/1748-9326/acbf6b.

632 Shi, J., K. Le, and B. Choi (2002), The pattern and seasonal variation of the
633 circulation in the region of the Kerguelen Plateau, *Acta Oceanologica Sinica*,
634 24(4), 11-22.

635 Smith, N. R., D. Zhaoqian, K. R. Kerry, and S. Wright (1984), Water masses
636 and circulation in the region of Prydz Bay, Antarctica, *Deep Sea Research Part*
637 *A. Oceanographic Research Papers*, 31(9), 1121-1147, doi:10.1016/0198-
638 0149(84)90016-5.

639 Sokolov, S., and S. R. Rintoul (2009), Circumpolar structure and distribution of
640 the Antarctic Circumpolar Current fronts: 1. Mean circumpolar paths, *Journal*
641 *of Geophysical Research-Oceans*, 114, doi:10.1029/2008jc005108.

642 Sparrow, M. D., K. J. Heywood, J. Brown, and D. P. Stevens (1996), Current
643 structure of the south Indian Ocean, *Journal of Geophysical Research: Oceans*,
644 101(C3), 6377-6391, doi:10.1029/95jc03750.

645 Stuecker, M. F., C. M. Bitz, and K. C. Armour (2017), Conditions leading to the
646 unprecedented low Antarctic sea ice extent during the 2016 austral spring
647 season, *Geophysical Research Letters*, 44(17), 9008-9019,
648 doi:10.1002/2017gl074691.

649 Swadling, K. M., S. Kawaguchi, and G. W. Hosie (2010), Antarctic
650 mesozooplankton community structure during BROKE-West (30°E–80°E),
651 January–February 2006, *Deep Sea Research Part II: Topical Studies in*
652 *Oceanography*, 57(9-10), 887-904, doi:10.1016/j.dsr2.2008.10.041.

653 Thompson, A. F. (2008), The atmospheric ocean: eddies and jets in the
654 Antarctic Circumpolar Current, *Philosophical Transactions of the Royal Society*

655 *a-Mathematical Physical and Engineering Sciences*, 366(1885), 4529-4541,
656 doi:10.1098/rsta.2008.0196.

657 Thompson, A. F., A. L. Stewart, P. Spence, and K. J. Heywood (2018), The
658 Antarctic Slope Current in a changing climate, *Reviews of Geophysics*, 56(4),
659 741-770, doi:10.1029/2018RG000624.

660 Trani, M., P. Falco, E. Zambianchi, and J. B. Sallee (2014), Aspects of the
661 Antarctic Circumpolar Current dynamics investigated with drifter data,
662 *Progress in Oceanography*, 125, 1-15, doi:10.1016/j.pocean.2014.05.001.

663 Turner, J., T. Phillips, G. J. Marshall, J. S. Hosking, J. O. Pope, T. J.
664 Bracegirdle, and P. Deb (2017), Unprecedented springtime retreat of Antarctic
665 sea ice in 2016, *Geophysical Research Letters*, 44(13), 6868-6875,
666 doi:10.1002/2017gl073656.

667 von Storch, J. S., C. Eden, I. Fast, H. Haak, D. Hernandez-Deckers, E. Maier-
668 Reimer, J. Marotzke, and D. Stammer (2012), An estimate of the Lorenz energy
669 cycle for the world ocean based on the 1/10 degrees STORM/NCEP simulation,
670 *Journal of Physical Oceanography*, 42(12), 2185-2205, doi:10.1175/jpo-d-12-
671 079.1.

672 Wakatsuchi, M., K. I. Ohshima, M. Hishida, and M. Naganobu (1994),
673 Observations of a street of cyclonic eddies in the Indian-Ocean sector of the
674 Antarctic Divergence, *Journal of Geophysical Research-Oceans*, 99(C10),
675 20417-20426, doi:10.1029/94jc01478.

676 Wang, G., H. H. Hendon, J. M. Arblaster, E.-P. Lim, S. Abhik, and P. van
677 Rensch (2019), Compounding tropical and stratospheric forcing of the record
678 low Antarctic sea-ice in 2016, *Nature Communications*, 10,
679 doi:10.1038/s41467-018-07689-7.

680 Webb, D. J. (1993), A simple model of the effect of the Kerguelen Plateau on
681 the strength of the Antarctic Circumpolar Current, *Geophysical & Astrophysical*
682 *Fluid Dynamics*, 70(1-4), 57-84, doi:10.1080/03091929308203587.

683 Whitworth III, T., A. H. Orsi, S.-J. Kim, W. D. Nowlin Jr., and R. A. Locarnini
684 (1985), Water masses and mixing near the Antarctic Slope Front, in *Ocean, Ice,*
685 *and Atmosphere: Interactions at the Antarctic Continental Margin*, edited, pp.
686 1-27, doi:10.1029/AR075p0001.

687 Williams, G. D., et al. (2016), The suppression of Antarctic bottom water
688 formation by melting ice shelves in Prydz Bay, *Nat Commun*, 7, 12577,
689 doi:10.1038/ncomms12577.

690 Williams, G. D., S. Nicol, S. Aoki, A. J. S. Meijers, N. L. Bindoff, Y. Iijima, S.
691 J. Marsland, and A. Klocker (2010), Surface oceanography of BROKE-West,
692 along the Antarctic margin of the south-west Indian Ocean (30–80°E), *Deep*

693 *Sea Research Part II: Topical Studies in Oceanography*, 57(9-10), 738-757,
694 doi:10.1016/j.dsr2.2009.04.020.

695 Wu, Y., Z. Wang, and C. Liu (2017), On the response of the Lorenz energy
696 cycle for the Southern Ocean to intensified westerlies, *Journal of Geophysical*
697 *Research: Oceans*, 122(3), 2465-2493, doi:10.1002/2016jc012539.

698 Zhang, Y., D. Chambers, and X. Liang (2021), Regional trends in Southern
699 Ocean eddy kinetic energy, *Journal of Geophysical Research: Oceans*, 126(6),
700 doi:10.1029/2020jc016973.

701